MDPI

Article

Using Ensemble of Hand-Feature Engineering and Machine Learning Classifiers for Refining the Subthalamic Nucleus Location from Micro-Electrode Recordings in Parkinson's Disease

Mohamed Benouis [1,†] and Alfredo Rosado-Muñoz [2,*,†]

1   Institute of Computer Science, Faculty of Applied Computer Science, University of Augsburg, 86159 Augsburg, Germany; mohamed.benouis@uni-a.de
2   GDDP, Department of Electronic Engineering, School of Engineering, University of Valencia, 46100 Burjassot, Spain
*   Correspondence: alfredo.rosado@uv.es; Tel.: +34-963543808
†   These authors contributed equally to this work.

Abstract: When pharmaceutical treatments for Parkinson's Disease (PD) are no longer effective, Deep Brain Stimulation (DBS) surgery, a procedure that entails the stimulation of the Subthalamic Nucleus (STN), is another treatment option. However, the success rate of this surgery heavily relies on the precise location of the STN, as well as the correct positioning of the stimulation electrode. In order to ensure the correct location, Micro-Electrode Recordings (MERs) are analyzed. During surgery, MERs capture brain signals while inserted in the brain, receiving different brain activity depending on the crossed brain area. The location of the STN is guaranteed when brain signals from MERs meet certain criteria. Nevertheless, MER signals are sensitive to various artifacts coming from machinery or other electrical equipment in the operating theater; patient activity; and electrode motion. These all lower the signal-to-noise ratio of the MER signals. MER signals are stochastic, multicomponent, transient, and non-stationary in nature, and they contain multi-unit neural activity in the form of spikes and artefacts. Thus, accurately defining that MERs are located in the STN is not an easy task. This work analyzes relevant features from MER, based on analyzing spike activity and local field signals. Six different classification algorithms are used, together with the optimal input feature selection. The algorithms are trained using supervised Leave-One-Out Cross-Validation. MER data were collected in a real scenario from 14 PD patients during DBS implantation surgery. The dataset is publicly available. The results derived from the use of this method show an accuracy of up to 100% in detecting where the MER electrode is located in the STN brain area.

Keywords: spike-dependent features; spike-independent features; machine learning; Subthalamic Nucleus (STN) detection; Parkinson's disease; Deep Brain Stimulation (DBS)

1. Introduction

Parkinson's disease (PD) is a dysfunction of the brain and nervous system that is linked to a loss of dopaminergic neurons. The diagnosis of PD accords to the existence of cardinal motor symptoms, which include bradykinesia, postural instability, tremor, and muscular rigidity. Other symptoms range from depression to sleep disorders, cognitive dysfunction, and language problems [1]. After Alzheimer's disease, PD is the second most prevalent neurodegenerative illness at present [2], affecting over 6.1 million people worldwide [3]. This would uphold the current interest in the development of efficient treatment. Pharmacology is the primary treatment option for PD [4], where the lost dopamine is replaced through the use of drugs such as Levodopa and Dopamine Agonists, albeit the success rate of this treatment usually decreases over time, and generally anti PD drugs are not tolerated well by the patient.

Most people with Parkinson's disease (PD) live in the community and are cared for by informal caregivers, including spouses, adult children, friends, or other unpaid individuals. However, caring for a partner or family member with PD negatively impacts the caregiver's own physical and emotional well-being and reduces their quality of life. In addition to the mental impact of caring for someone with Parkinson's disease (PD), caregivers often face an economic burden and sometimes financial hardship. Beyond the increased financial costs of caring for someone with PD, caregivers are also likely to experience reduced productivity at work due to absenteeism, disability, or forced retirement. Estimates indicate that PD caregivers have a higher cumulative income loss over five years compared to control subjects [5].

Deep Brain Stimulation (DBS) surgery of the STN, Pedunculopontine Nucleus (PNN), and Globus Pallidus Internus (GPi) is the most popular surgical treatment to improve motor skills in patients with PD and Freezing of Gait (FoG) who do not improve using the pharmacological treatment or have side effects to it [6]. The surgery procedure of DBS implantatoin is an expensive and complicated surgery. It consists of the insertion of MERs and stimulation electrodes from the brain surface to the STN location. Once in STN brain area, the stimulation electrode is fixed and a stimulation signal is applied (in a similar way to a pacemaker), blocking the PD movement disorders' symptoms. The fail risk factor of surgery remains an important issue since an improper location of the stimulation electrode will not block PD symptoms. Improving the efficacy of DBS-STN surgery by examining the brain morphology structure and the volume of tissue has become an important issue [7], as well as the optimal fixation of the stimulation electrode. However, given that the STN is quite a small area inside the brain, imaging methods as Magnetic Resonance Imaging (MRI) or Computed Tomography (CT) only serve as initial guides for trajectory definition from the brain surface to the STN region [8]. Surgeons are faced with the difficult task of the correct placement of the stimulating electrodes. The location of the STN and its borders is normally carried out manually (the visualization of the MER signal in a monitor) by a neurosurgeon and is a complicated, arduous task. It has been reported that incorrect placement can result in adverse side effects such as mood disorders [9]. Therefore, the careful and correct localization of the STN during this surgery is paramount. As a result, the accurate placement of the electrode within the dorsolateral sensorimotor part of the STN is considered necessary for a satisfactory outcome [10,11].

Several statistical methods have been applied to detect the entry and exit of the STN region, along with the optimal depth for electrode implantation through the use of MER signals. Two main feature extraction groups have been developed in this study in order to identify the neural background activity of the STN region [12]. In the first group, spike-dependent features were chosen as the basis because they describe explicit information known as the firing rate; indexing firing; and potential field information being extracted from either time-domain or frequency-domain representations. However, methods operating upon spikes either amplitude or time spike segments are often susceptible to intra/inter variabilities induced from non-stationary MERs' signal nature and their environment acquisition, thereby leading to poor STN location classification and clinical outcomes [13]. In the second group, spike independence can be also used to classify non-stationary signals by extracting only relevant local field information features. They can be extracted in a number of ways, e.g., by dividing a signal into a number of segments and computing the features in each segment-based feature such as statistical or frequency information [14]. Spike-independent features employ time-frequency signal representation to explore the main MER activity hidden in the high- and low-frequency bands. Unfortunately, the use of such a method requires prior information of firing spike activity, and its relation to PD symptoms variations remains unknown in the cognitive neuroscience field [15].

These manual methods make it difficult to obtain a feature extraction method capable of capturing the deep characteristics needed to clearly point to the location of the STN region. For this reason, machine learning techniques have been effectively employed for the validation of the planned directions in the procedure of DBS surgery to obtain the

correct position of electrodes inside the brain and determine the STN location. The wavelet method is used in [16]. Learning techniques such as linear discriminant analysis are used in [17]. K-nearest Neighbors (KNNs), Support Vector Machines (SVM) [18], and decision trees [19] are also used. But the most used techniques in the bibliography are Neural Networks (NNs) [20] and SVM [21]. In this paper, we show how a sparse representation of MER signals allows for the extraction of discriminant features, improving accuracy in the identification of STN during DBS surgery applied in patients with Parkinson's disease. We use spike-independent and spike-dependent features extracted from MER. The extraction and selection of the features can then be applied to machine learning classifiers. Thus, the main objective of this work is to assess the improvement of the classification performance when dealing with STN brain structure detection. A wide number of features and classification algorithms are described, achieving high accuracy in STN area detection.

The remainder of this paper is organized as follows. Section 2 introduces the dataset, explains the proposed methodology, and details the used classification procedure: noise cancellation, baseline removal, and segmentation as preprocessing. Section 3 describes the feature extraction and selection. Section 4 outlines the classification procedure and parameters used to evaluate the performance of the classification. The results of the analysis and a discussion of these are presented in Sections 5 and 6, respectively. Finally, Section 7 concludes the paper.

2. Materials and Methods

In this study, MER data were recorded from the electrophysiological exploration of idiopathic PD patients during DBS surgery in 'La Fe Hospital' of Valencia University, Spain. Prior to surgery, imaging techniques estimated the brain target area (STN) and optimal trajectories (bilaterally) to reach the STN. During the surgery, MER electrodes advanced in 0.2 [mm] steps, with several seconds acquisition in each step. Acquisition started 5.8 [mm] before and 0.4 [mm] after reaching the estimated STN target area. Due to surgery conditions, some were inserted in both hemispheres (bilaterally) or either right or left (see Table 1 with details for each patient). The collected data, sampled at 12 kHz, comprised a total of 830 recordings obtained from 14 patients (9 males and 5 females; age: 65.1 ± 5.6 years). Each MER recording corresponded to a different depth and brain lobe. For each patient, the number of steps (depths) varied (see Table 1). For each step, three acquisition channels could be used, but due to surgical practice, only one or two channels were acquired. In this work, the second channel was the only one used. Data were classified into two classes: STN-IN and STN-OUT, as in similar works [12], without considering the depth in which it was acquired. The average duration for each step in STN-IN, for the left and right lobes, was 51.0 s and 46.8 s, respectively, and the average duration for each step in STN-OUT, for the left and right lobes, was 46.3 s and 42.1 s, respectively. Each step was classified within the STN-IN or STN-OUT class by expert surgeons during the surgery process.

For each acquired depth, MER data were segmented using 1 s segment duration with 50% overlapping. In total, 78,611 MER segments were obtained: 30,140 for left STN-IN, 22,725 for right STN-IN, 17,030 for left STN-OUT, and 8716 for right STN-OUT, respectively. The dataset is publicly available in ZENODO [21].

Figure 1 shows the DBS surgery process in six steps. With the patient under general anesthesia, an orifice is made in the skull, a cannula is inserted, and it is verified that the inserted position is adequate to reach the estimated position of the STN. Second, the initial target position is traced. Third, MERs are inserted and a verification that MERs are inserted is made. When MERs are inserted and the signal obtained is analyzed, the decision on the best position of the stimulation electrode is made (step 4). Finally, the stimulation electrode is inserted and the verification of stimulation is made before its final fixation (steps 5 and 6). Figure 2 shows an image of the process of CT imaging and the use of a stereotactic robot with a fiducial point to define the trajectory.

Table 1. Microelectrode (MER) data recordings. Fourteen patients in total, acquired in one or both brain lobes, at a different number of depths (steps). For each patient, the number of steps and total seconds acquired are shown.

| Patient Number	STN-IN(L+R) #Steps	STN-OUT(L+R) #Steps	STN-IN(L+R) Seconds	STN-OUT(L+R) Seconds	Total Seconds
1	20+NA	4+NA	959+NA	134+NA	1093
2	18+31	14+3	1354+1855	591+199	3999
3	13+27	27+12	626+993	923+434	2976
4	21+21	11+9	946+1114	629+421	3110
5	26+NA	15+NA	1200+NA	497+NA	1697
6	15+NA	25+NA	941+NA	1528+NA	2469
7	23+NA	7+NA	1632+NA	731+NA	2363
8	22+17	11+26	1229+1041	454+1141	3865
9	30+37	8+4	1248+1322	285+114	2969
10	32+32	15+13	1147+1852	921+557	4477
11	18+NA	19+NA	1024+NA	939+NA	1963
12	30+30	11+12	1415+995	380+416	3206
13	29+25	18+14	1429+1119	548+640	3736
14	NA+24	NA+11	NA+1129	NA+461	1590
TOTAL	297+244	185+104	15,150+11,420	8560+4383	39,513
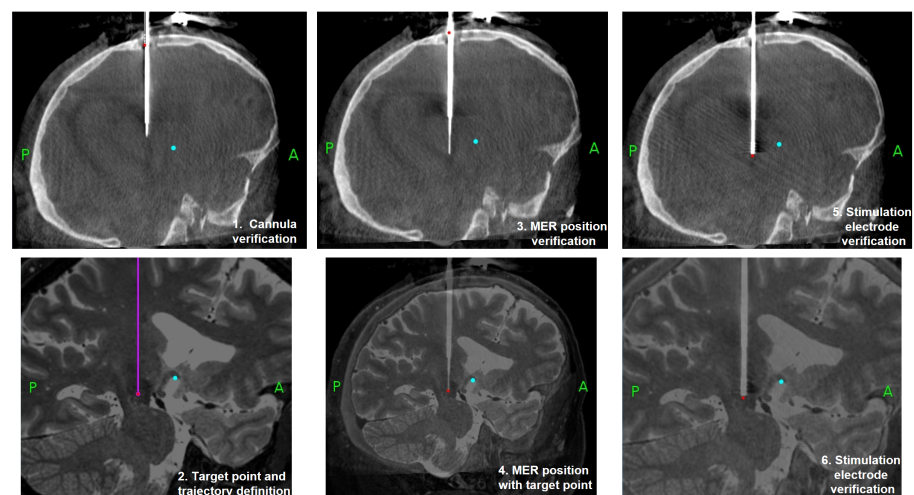
Figure 1. DBS surgery process and MER signal acquistion according to the positions where the MER electrodes are displaced.

Figure 2. DBS Surgery process. The patient is fully sedated with anesthesia, head fixed with a stereotactic frame. Intraoperative CT is used for image acquisition at different surgery moments. A stereotactic robot with fiducial end-point tool to define fiducial points (five red balls) and reference trajectory point for incision (red laser light) is used.

An example of MER traces recorded along the pre-planned trajectory is displayed in Figure 3. Neural activity recorded in the pre-STN, STN, and post-STN regions is shown with respect to the expert annotation. These annotations are generally carried out manually and represented in depths (distance in mm) with respect to the Estimated Distance to the Target (EDT).
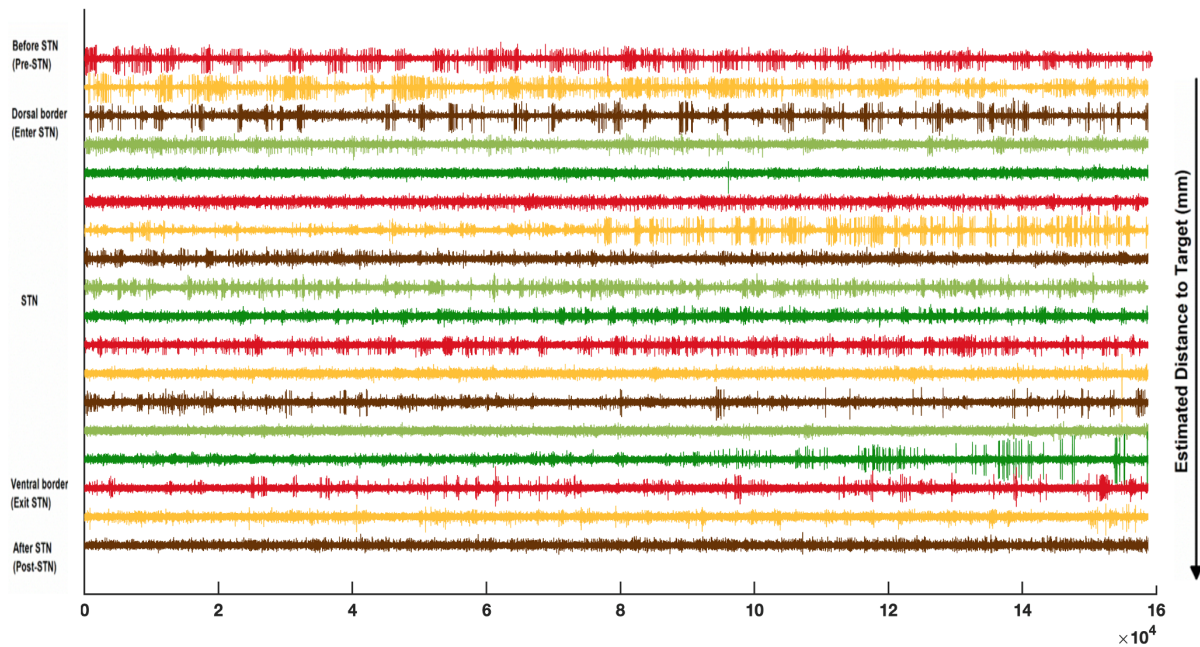

Figure 3. Example of MER signals recorded at various depths along the trajectory from a patient with Parkinson's disease from outside STN (pre-STN), inside STN, and outside STN (post-STN).

Finally, prior to the use of the data segments for feature extraction, a high-pass filter was used to eliminate the main artifacts and noise was used. In this case, a band-stop filter was used to remove the 50 Hz noise, together with two Butterworth filters (4th-order) with a cut-off frequency of 0.5 Hz for the first filter and lower and higher cut off frequencies of 48 Hz and 52 Hz, respectively, for the second filter.

Alpha-Omega® equipment was used: MER electrodes, the microelectrode and Local Field Potential Register with the automatic neuro navigation system, and the motorized electrode driver.

3. Feature Extraction

A combination of features is proposed. Since the neuron activity in the brain is based on spikes, and different brain areas provide different spike patterns, a subset of features is taken from the spike activity. A second subset of features measuring the Local Field Potential (LFP) activity was also used. These features do not directly measure spike activity but they provide information about the neural activity in areas near the MER electrodes. All extracted features (f_j) were normalized according to Equation (1), where F_j is the normalized feature.

$$F_{j,i} = \frac{f_{j,i} - f_{j,\min}}{f_{j,\max} - f_{j,\min}} \tag{1}$$

3.1. Spike-Dependent Features

Seven features related to spikes appearing in MER segments were extracted, as illustrated in Table 2 [22]. All feature equations are detailed in Appendix A.

Table 2. Spike-dependent features obtained from MER segments.

Features	Description
Spike Firing Rate (SFR)	Count of spikes per second.
Inter Spike Interval (ISI)	Time intervals between consecutive spikes in the spike sequence [23].
Standard deviation of *ISI* (SISI)	Standard deviation of inter-spike intervals *ISI*.
Pause Ratio (PR)	Ratio of cumulative time of *ISI* greater than 50 ms to the cumulative time of ISI less than 50 ms.
Pause Index (PI)	Ratio of the number of *ISI* greater than 50 ms to the number of *ISI* less than 50 ms.
Bursting Rate (BR)	Number of bursts per second.
Modified Burst Index (MBI)	Ratio of the number of *ISI* less than 10 ms to the number of *ISI* greater than 10 ms.

3.2. Spike-Independent Features

These features measure the LFP activity in MER segments and are mainly based on statistical, temporal, and spectral properties [24–26]. Each feature is computed for the 1 s MER segments. The list of features and their description is shown in Table 3. Detailed equations are shown in Appendix B.

Table 3. List of spike-independent features based on the analysis of 1 s MER segments.

Features	Description
Bispectrum (Bs)	The Fourier transform of the third-order cumulant spectrum [25].
Zero crossing (Zc)	Number of zero crossings in the temporal domain [24].
Curve length (Cl)	Sum of the difference of consecutive samples [27].
Integrator (In)	Sum of absolute value [24].
Root Mean Square (RMS)	Root mean square [24].
Kurtosis (Ku)	Peakiness coefficient variation [28].
Cumulative bispectrum (Cb)	Cumulative relationship between the higher-order moments [25].
Average Amplitude Change (AAc)	Average value of all amplitudes [24].
Short-Term Fourier Transform (STFT)	Spectrum energy from each MER segment [29].
Teager Energy (Te)	Energy rate induced from the second-order differential derivative of the amplitude and frequency variation [30].
Average First Amplitude difference (AFa)	Average of first amplitude difference [24].
Second Amplitude difference (SAd)	Average of second amplitude difference [24].
Standard deviation (SD)	Standard deviation [24].
Skewness (Sk)	Measure to quantify the presence of assymetry in the shape of the distribution [31].
Slope Sign change (SSc)	Number of times that the slope of the MER curve changes its sign in the segment [24].
Variance (Va)	The signal's averaged power [24].
1D-Local Binary Pattern (LBP1)	Having the central segment as threshold, it is compared with its neighborhood to generate binary code [32,33].

As an example, Figure 4 displays bispectrum (Bs) plots of STN-IN and STN-OUT MER segments. The bifrequency magnitude distinguishes between each class. Also, most of the

magnitude of the bispectrum lies within -0.01 to 0.01, and there is a random distribution of the magnitudes at various frequencies.
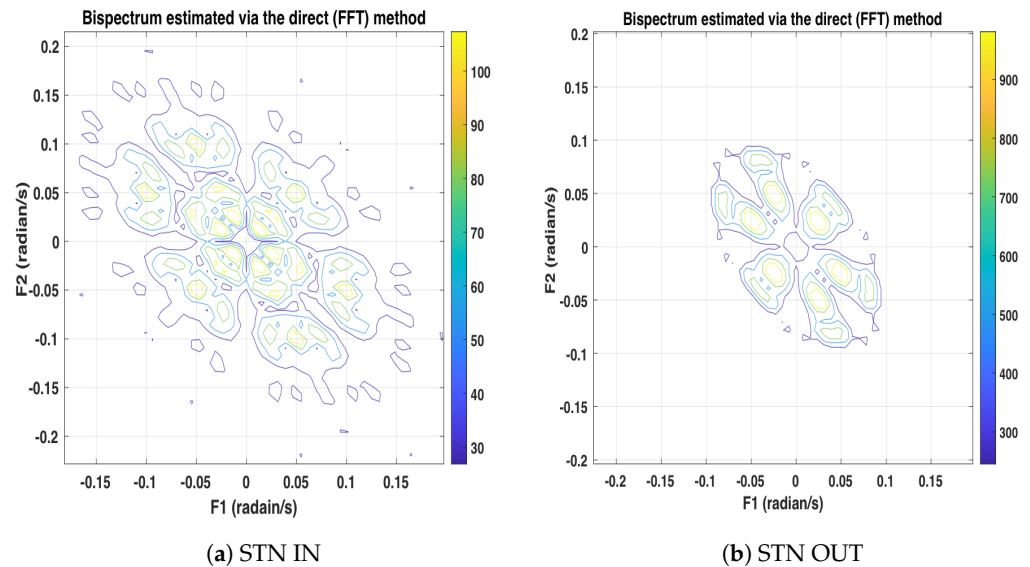

(**a**) STN IN   (**b**) STN OUT

Figure 4. (**a**) Bispectrum plot of the mean of 10,000 randomly selected MER segments in STN-IN. (**b**) Bispectrum plot of the mean of 10,000 randomly selected MER segments from STN-OUT.

3.3. Feature Reduction

Feature reduction eliminates some features, reducing the computational complexity of the classifier and avoiding the possibility of redundancy. Initially, we obtained 24 features aimed at two class classification (STN-IN and STN-OUT). Many feature selection methods exist: Particle Swarm Optimization (PSO), Genetic Algorithms (GAs), Independent Component Analysis (ICA), Butterfly, Firefly, Ant Colony, Harris Hawks optimizations methods, etc. In this work, the NCA (Neighborhood Component Analysis) selection method is used, which automatically selects the most meaningful features [34]. The steps of the NCA-based feature selector are given below. Thus, by having a threshold value ($th = 0.5$), the complete set of features is entered and the final result of the algorithm provides the most relevant features. The NCA sorts the best features from the diagonal matrix that is constructed by maximizing the objective function that computes the average leave-one-out classification over the training set. The main steps in the NCA algorithm are the following:

- Step 1. Using weight calculate the function to generate the weights W_{NCA} as defined in Equation (2). M_{feat} and T_{feat} are two feature observations randomly selected from the database.

$$W_{NCA} = F\left(M_{feat}, T_{feat}\right) \qquad (2)$$

where $F\left(M_{feat}, T_{feat}\right) = \sqrt{\left(M_{feat} - T_{feat}\right)^T D(M_{feat} - T_{feat})}$ and D is a semi defined matrix [34].

- Step 2: Sort feature weights in descending order.
- Step 3: Select the most distinctive k features by using the highest positive weights according to the threshold values (greater and equal than 0.5).

After completing the NCA process, a reduction in features of 45% was obtained, i.e., 11 out of 24 features were selected as relevant. It is important to note that 10 out of the 11 selected features belong to spike-independent features—Spike Firing Rate (SFR) for spike-dependent, with the rest are from spike-independent features: Cumulative bispectrum (Cb), Skewness (Sk), Bispectrum (Bs), 1D-Local Binary Pattern (LBP1), Variance (Va), Short-Term Fourier Transform (STFT), Standard deviation (SD), Root Mean Square (RMS), Teager Energy (Te), and Slope Sign change (SSc).

In summary, the proposed classification procedure is depicted in Figure 5: the acquired MER signal is segmented in 1 s time window and preprocessed for artifact and noise removal; then, different features (spike- and non-spike-dependent) are extracted (24 in total). After that, the NCA feature reduction algorithm is used, obtaining 11 relevant features that will be used as the input to a machine learning classifier, which provides the two classifications (STN-IN and STN-OUT).
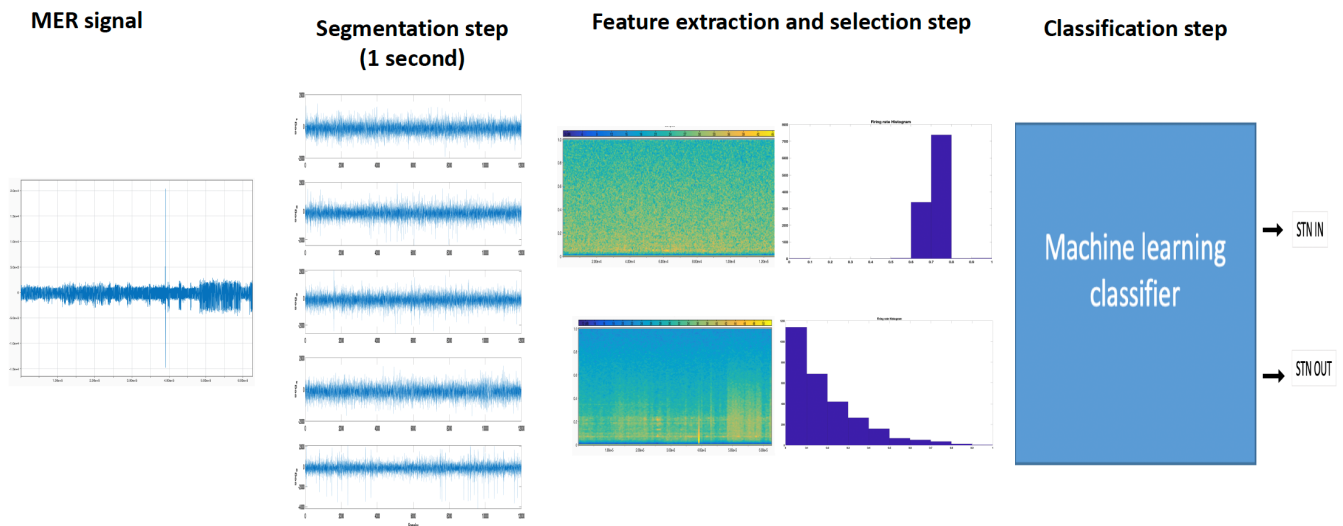

Figure 5. Global procedure for the proposed method for STN localization based on MER signals: from signal acquisition to classification.

4. Classification Procedure and Performance Evaluation

A supervised classification approach was employed via ensemble classification models developed in MATLAB (2021b) (Statistics and Machine Learning toolbox). Each model was trained using the following configuration [35].

- Support Vector Machine (SVM). As already stated, the SVM classifier has shown a good achievement for the STN location based on MERs or LFP data within various scenarios. In this work, the configuration model was chosen to avoid the risk of overfitting. Accordingly, a Radial Basis Function (RBF) kernel function was used, with the kernel scale set to 1 and constraint penalty set to 1.
- K-Nearest Neighbors (KNNs). In this study, the malhabonic distance metric is used to compute the distance between the test feature and training features belonging to M classes (in this case, M = 2), and each data input will be assigned into a specific class based on the minimum computed distance between the test data and K (in this case, K = 5) nearest training data.
- Random Forest (RF). Random Forest is a set of decision trees constructed to train each subgroup out of the whole data training set at each decision tree and then deliver a single decision that will be aggregated with all decisions to output the predicted class index. In this work, after the optimization process, each classifier has been set to 32 trees with a leaf size equal to 4.
- Decision Tree (DT). In the decision tree classifier, the decision rule is made up of the features outcome learned by three compromised principal nodes: root node, decision node, and leaf node, which handle the extracted features, the branches' decision outcome, and the predicted class (STN IN and STN OUT), respectively.
- Discriminant Analysis (DA). In this algorithm, the input features are separated by a discriminate linear plane engendered from the estimation of the covariance matrix rate [22]. The DA plan aims at minimizing the variance of the features that belong to the same class and maximizing the variance of features between classes (STN-IN and STN-OUT).

- Neural Network (NN). Among multiple variants, we used three families of neural networks: the Probabilistic Neural Network (PNN), Feed-forward Neural Network (FNN) and Back-propagation Neural Network (BNN). For all of them, they comprise at least three layers: the input layer, the hidden layer, and the output layer. For training, the Stochastic Gradient Descent (SGD) is used. The topology consists of a single hidden layer with 28 units, and the last layer is softmax of two classes (STN-IN and STN-OUT).

For all models, the 'Leave-One-Out Cross Validaton' (LOOCV) training method was used, i.e., each classifier model was trained on observations from 13 patients, while data from the 14th patient were used for validation, obtaining a total of 14 different models for each combination of conditions. Different statistical methods were used to estimate the performance: the ROC curve, the confusion matrix, accuracy, recall, precision (Equation (3)), the F-measure (Equation (4)), and the kappa coefficient (Equation (5)), where T_p, T_n, F_p, F_n, T, and P represent the number of true positives found, true negatives found, false positives found, false negatives found, total number of actual true positives, and total number of actual true negatives, respectively.

$$accuracy = \frac{T_p + T_n}{T} \quad ; \quad recall = \frac{T_p}{P} \quad ; \quad precision = \frac{T_p}{T_n + F_p} \tag{3}$$

$$F_{measure} = \frac{2 * (precision * recall)}{(precision * recall)} \tag{4}$$

$$Kappa = \frac{2 \times (T_p + T_n - F_n \times F_p)}{(T_p + F_p) \times (T_n + F_p) + (T_p + F_n) \times (T_n + F_n)} \tag{5}$$

5. Results

A comparison between the classifiers described above, and the difference between the complete feature set and the reduced input set, is made.

Table 4 shows the accuracy results. Results with the reduced feature set are similar to those achieved with all features, confirming that the feature reduction method neglected the redundant features and was able to preserve the relevant features able to distinguish STN-IN and STN-OUT classes. Actually, when using all 24 features, the average performance decreases due to redundancies and higher confusion among features. Thus, the rest of results focus on the reduced set of features (11 features).

Table 4. STN localization accuracy comparison between the reduced feature set and the complete feature set.

| ML Classifier	KNNs	SVM	RF	DT	DA	PNN
The 11 features selected	99.9	100.0	99.9	99.8	100.0	100.0
All 24 features selected	99.8	99.9	99.5	99.9	99.8	100.0

The results were individually analyzed for each patient. Despite each patient being anatomically different, Table 5 shows that the classification results ranged from 99% to 100%, except for patient 3, with 96%.

Concerning the ROC curves, Figure 6 shows a very narrow area, with all classfiers having similar behavior. This is also supported by the confusion matrices shown in Figure 7. All classifiers achieved a similar accuracy, ranging from 99% to 100%.

An analysis of features was also carried out in order to evaluate if spike-dependent (SD) or spike-independent (SIN) features have an impact on the result. For this analysis, the PNN classifier was used. Thus, a set of 3 and 7 SD features were randomly chosen, while keeping 14 SIN features. Then, four trials were made by using 3, 7, 14, and 17 SIN features with no SD features. Figure 8 shows the accuracy results.

Table 5. Performance indices individualized per patient using PNN classification and the reduced set of features.

Patient	Precision	Recall	Kappa	F1-Score	Accuracy
P1	100	100	86.8	100	100
P2	100	100	87.0	100	100
P3	86.9	95.1	87.7	90.1	96.3
P4	100	99.9	84.9	99.9	100
P5	96.6	99.6	87.9	98.0	99.5
P6	99.8	99.8	84.4	99.8	99.9
P7	99.8	99.8	84.8	99.8	99.9
P8	99.8	99.9	88.4	99.3	99.6
P9	98.8	99.9	88.4	99.3	99.6
P10	99.6	99.5	81.2	99.5	99.6
P11	99.8	99.8	80.8	99.8	99.8
P12	99.7	100	86.1	99.8	99.9
P13	99.7	100	86.1	99.8	99.9
P14	99.5	99.9	87.0	99.6	99.7
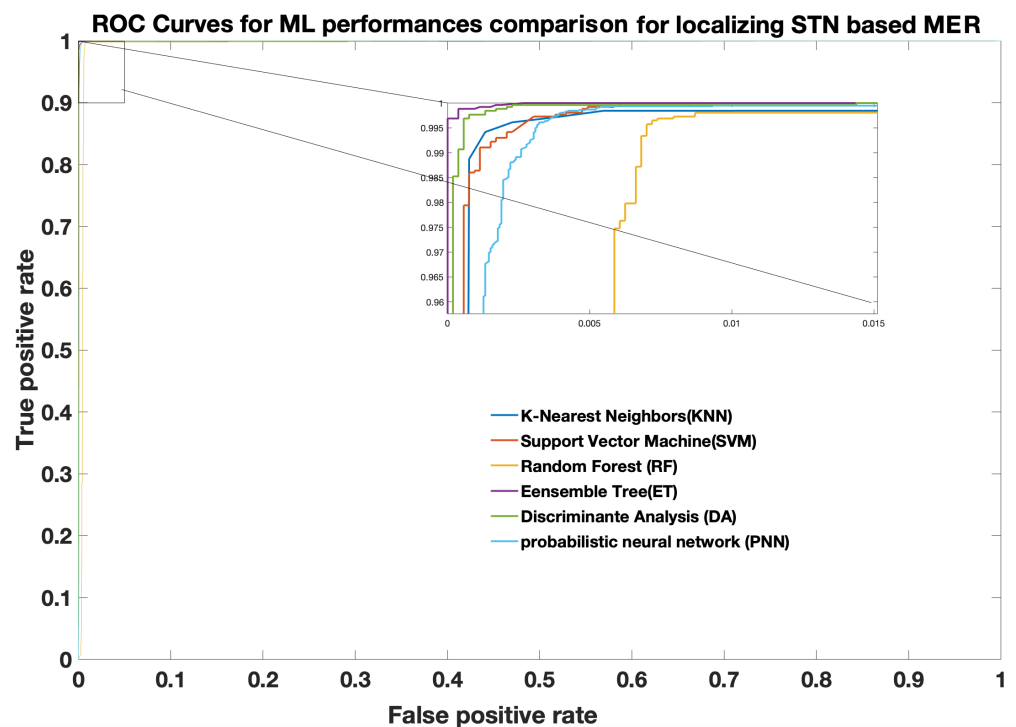
Figure 6. ROC curves for all the classifiers used in this work for STN-IN and STN-OUT area detection.

As already obtained by the NCA feature reduction algorithm, it is clear that SIN features are more relevant for the correct detection. However, it is not necessary to use most of the SIN features since a reduced set provides successful classification ratios while reducing computational cost.

As an example of the class separation provided by the chosen features, Figure 9 shows the scatter plot for *Sk* and *SD*, showing that they can separate the STN-IN and STN-OUT classes. The remaining scatter plots are shown in Appendix C. Thus, scatter plots for the other selected features are also shown, which show a clear distinction. Some other features show overlapping areas, which means that they should be plotted in higher dimensions, they are non-linearly separable, or outliers exist.
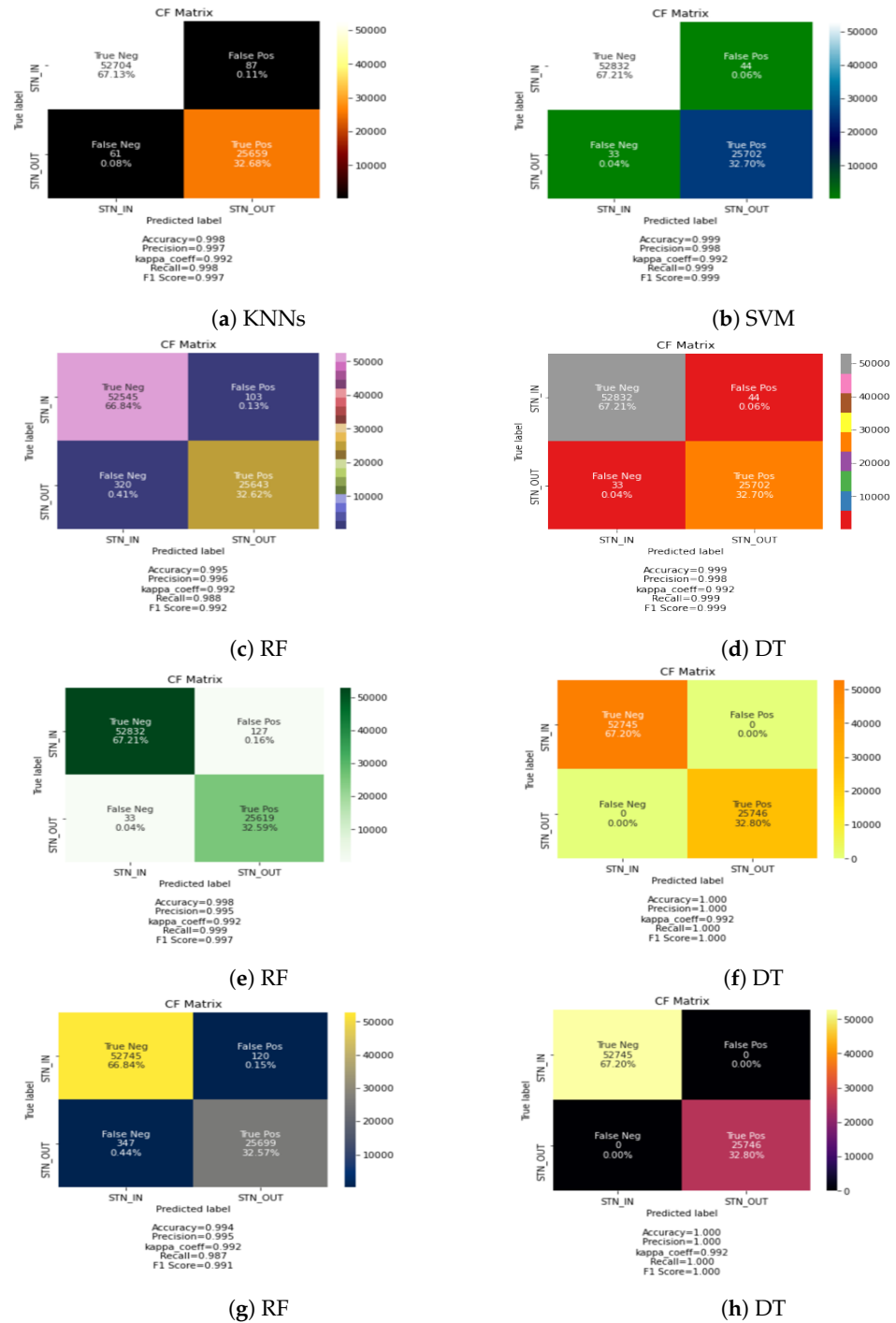
Figure 7. Confusion matrix for the ML classifiers. (**a**) KNNs. (**b**) SVM. (**c**) RF. (**d**) DT. (**e**) DA. (**f**) BNN. (**g**) FNN. (**h**) PNN.

A visualization of the feature space formed by the two features selected using NCA for STN target localization is shown in Appendix C. The spectral features show a clearer separation compared to other SIN features due to the use of band frequency characteristics. In addition, a nonlinear feature provides better detection of the relevant spiking activity of STN neurons and reduces sensitivity to outliers. Then, statistical features are ideal for capturing linear or periodic variation, and the Cumulative bispectrum is ideal for detecting irregular spiking activity induced along STN borders.
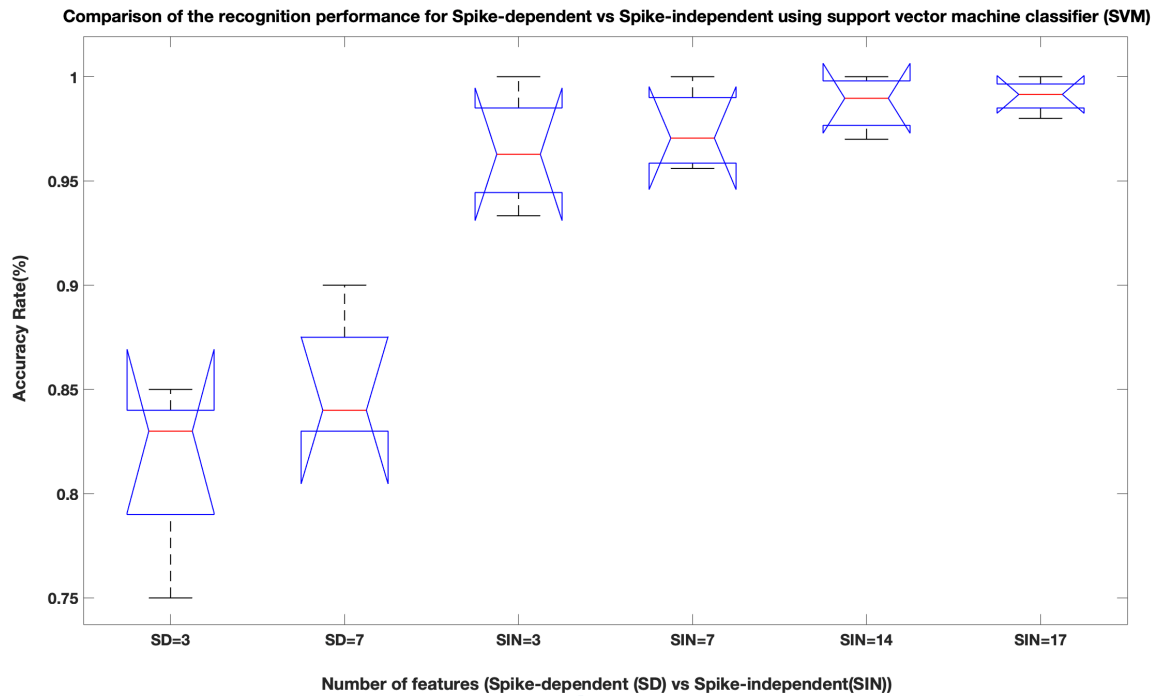
Comparison of the recognition performance for Spike-dependent vs Spike-independent using support vector machine classifier (SVM)

Figure 8. Comparison of STN area detection accuracy with PNN by using different combinations of spike-dependent (SD) and spike-independent features (SIN).
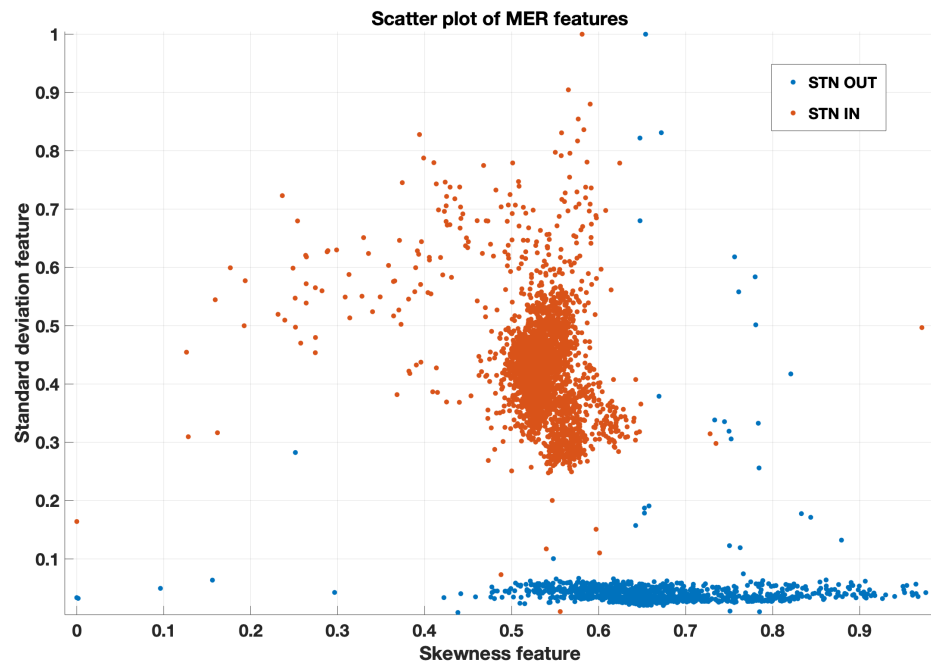

Figure 9. Scatter plot of Skewness (*Sk*) and Standard Deviation (*SD*) features extracted from MER segments (patient 1). STN-IN and STN-OUT classes are mostly separated.

Previous studies have shown that MER signals are non-stationary and that STN borders can be modeled as high-background electric activity zones with some artifacts, where the number of firing spikes depends on the area zone of the basal ganglia [19,36]. These observations about background patterns have already been demonstrated in clinical trials where the surgeon can discriminate among basal ganglia areas by listening to the audio variation that occurred. This is related to the frequency distribution of the signal. Figure 10 shows an example of spectrum energy representations (STFT) from the STN-

IN and STN-OUT areas: an irregular distribution variation in STN-IN, and a regular distribution variation in STN-OUT exists.

Our study is compared with recent existing works. The main difference between the accuracy of the proposed model and other works on the STN target localization is based on the data settings, preprocessing step, the type of handcraft features, and the classifier chosen. The comparison results are shown in Table 6.
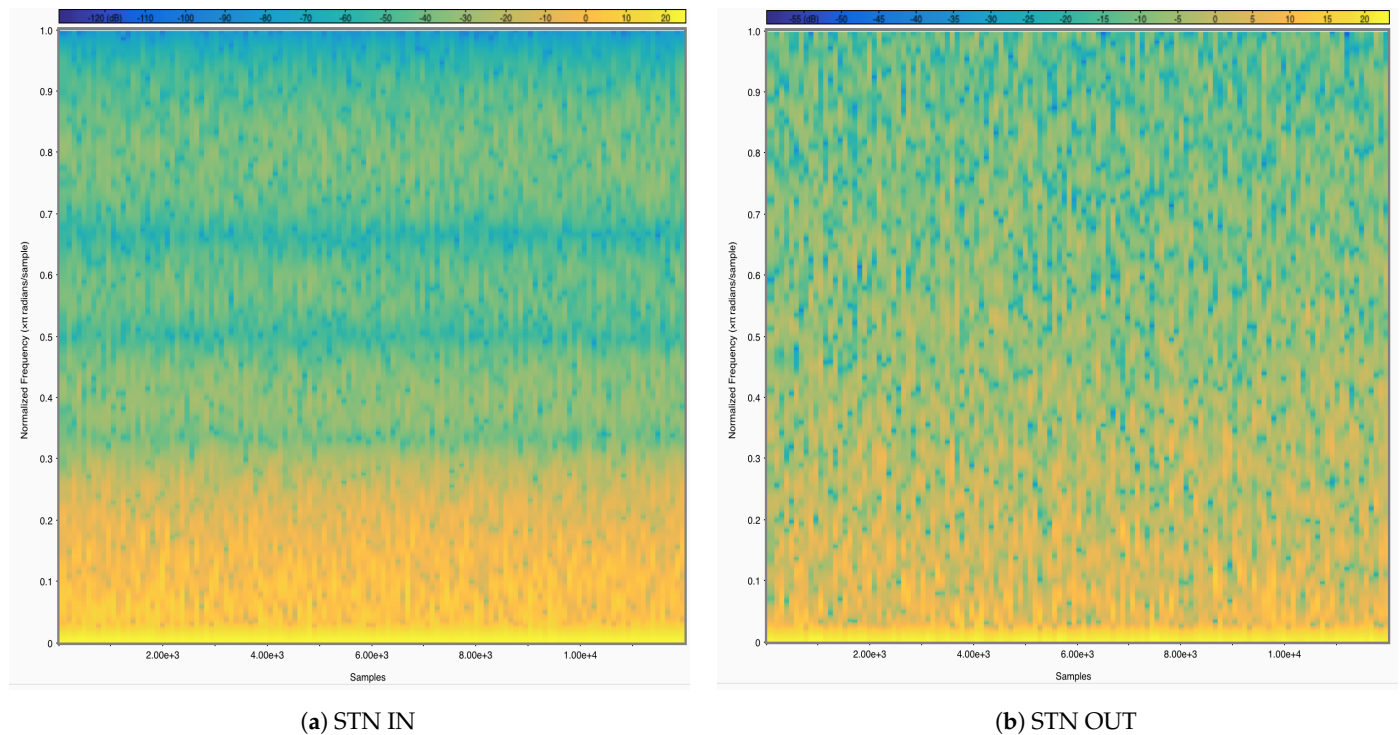

(**a**) STN IN

(**b**) STN OUT

Figure 10. Spectrum energy plot (STFT) for 12,000 randomly selected MER segments in STN-IN (**a**) and STN-OUT (**b**).

Table 6. Comparison of algorithms used for STN detection: authors, number of patients used, number of features, classifier, training method, and accuracy result.

Authors	# Patients	# Features	Classifier	Training	Accuracy (%)
Wong et al. [37]	27	13 SD and SIN	Fuzzy clustering	Hold-out	89.6
Cangan et al. [38]	48	3 SD and SIN	Unsupervised	NA	88.0
Chaovalitwongse et al. [36]	17	3 SD and SIN	Bayesian, KNNs, and KNNs-DTW	LOOCV	89.6
Guillen et al. [39]	4	6 SIN	SVM	10-fold CV	99.4
Vargas Cardona et al. [40]	4	3 SD and SIN	Bayesian and KNNs	NA	85.0
Rajpurohit et al. [18]	26	13 SD and SIN	Logistic regression	10-fold CV	84.0
Schiaffino et al. [41]	8	15 SD and SIN	KNNs and Fuzzy KNNs	LOOCV	72.0
Schiaffino et al. [42]	15	16 SD and SIN	KNNs	10-fold CV	86.1
Valsky et al. [43]	81	2 SIN	SVM and HMM	10-fold CV	94.0
Bellino et al. [44]	14	18 SD and SIN	KNNs	LOOCV	94.4
Karthick et al. [14]	26	1 SIN	Random Forest	LOOCV	83.0
Khosravi et al. [45]	50	1 SIN	K-means clustering and SOM	k-CV	80.0

Table 6. *Cont.*

Authors	# Patients	# Features	Classifier	Training	Accuracy (%)
Khosravi et al. [46]	100	11 SD and SIN	Deep Neural network	10-fold CV	92.0
Karthick. et al. [47]	26	1 SIN	Random Forest, SVM, and KNNs	LOOCV	94.0
S Coelli et al. [48]	13	26 SD and SIN	Decision trees	LOOCV	94.1
Hosny et al. [19]	21	12 SD and SIN	Bagging, KNNs, SVM, Decision Tree, and AdaBoost	LOOCV	94.8
Our work	14	11 SD and SIN	SVM, KNNs, RF, DT, DA, and NN	LOOCV	99.8

6. Discussion

If adequate imaging methods as MRI-guided and stereotactic CT-verified techniques are used in DBS surgery, no additional support tools need to be used [49]. However, the use of MERs is widely accepted during DBS surgery in order to validate the imaging methods and provide more information to the surgeon. In addition, MER signal analysis has proven to provide neuronal biomarkers to discriminate between the different brain structures located from dorsal to ventral STN borders. Recent studies detecting STN have employed feature selection methods for machine learning classifiers in order to increase the detection of the STN area [12], proving that the immediate information provided by the algorithm can support the medical team to improve clinical decision-making, together with surgeon criterion and imaging techniques [50].

In general, the results show that the proposed classification procedure, using the adequate features, can provide an accurate detection of the Subthalamic Area (STN-IN). The final set of 11 features mostly comprised those obtained from the Local Field Potential (LFP) using time, frequency, and higher-order statistics features.

It is important to note that spike-dependent (SD) features are less relevant that spike-independent (SIN) features. This result indicates that Local Field Potential features provide enough information with which to discriminate between different brain structures, and the spike activity might depend on other factors rather than the brain structure (e.g., patient mental activity). This finding accords with previous results from STN recordings in PD [51]. Despite this general finding, further analysis should be made on spike activity as it might provide more information about the patient, not only related to the brain structure where the spike activity is located.

High-order statistics are found to be the most discriminant feature group. Although the calculation of nonlinear frequency features is computationally expensive compared to the statistical temporal features, they must be used as long as the compation time does not exceed the feedback time (several seconds) given to the surgeon during the DBS implantation operation. In terms of clinical use, providing the surgical team with a real-time tool is a must for this type of algorithm as it is intended to be used online while the DBS operation is being carried out. Since the algorithm was developed using Matlab software, we developed a self-executable program ready to be run in the surgical room by a computer with access to MER acquisition channels.

For the classification task, Machine Learning (ML) techniques have shown to be a lightweight model classification compared with Deep Learning (DL) techniques due to the requirement of resources and data availability. As a result, focusing on MER signal classification using ML to detect the STN anatomical boundaries has similarly been on the rise. In this work, we explore the ability of ML to train handcrafted features from MER signals regarding the STN region detection.

Recent studies have shown the ability of handcraft feature selection methods to increase the detection of STN borders [12]. Several studies have proposed methods for STN

localization using deep learning methods [17,20,52]. However, lack of data availability is identified as one of the main barriers to implementation as clinicians should be confident that the algorithm outcome can be trusted. Moreover, it is common that research teams do not share their dataset for real MER data, which limits the possibility of comparison when developing new algorithms. In this work, we have developed our own patient's database, and it is available through open data repositories.

In summary, STN can be effectively detected, as this work shows. However, an open research topic exists when determining the optimal stimulation location inside the STN structure. It is still uncertain which features could reveal significant information regarding different areas inside the STN. Several linear and frequency-domain techniques have been used to analyze the MER signals and define new signatures of the STN region in PD patients. However, such techniques are ineffective in quantifying the spikes and background activity in MER signals in different depths and locations inside the STN due to their complex nature, correlation among neuron activities, and brain activity situation. Therefore, the neurosurgeon must always take the final decision using all possible available tools (imaging, signal analysis, and subjective experience).

An extension to this work is related to the number of patients used for the algorithm development. Despite the fact this work uses a number of patients—in line with other works—it is desirable to increase the number of patients. As new DBS surgeries are being carried out by the neurosurgical team, new data are acquired and then incorporated into the database.

7. Conclusions

Deep Brain Stimulation (DBS) has been shown to be an invasive technique greatly improving quality of life for PD patients. However, the success of DBS sugery greatly depends on the precise implantation of the stimulating electrode in the motor area inside the STN brain region. It is a key factor for optimal therapeutic benefits and the avoidance of side effects.

In addition to imaging and carefully planned trajectories in pre-surgical studies, this works describes the use of MER signals to support the surgeon in the analysis of brain signals during the surgery and optimally determine the final positioning of stimulating electrodes inside the STN. Without additional support, the process is instinctive and laborious for the neurosurgeon. The proposed classification algorithm is intended to be used in the operation theater and to provide information to the surgeon about the location of MERs and stimulating electrodes in the STN brain area. This work proposes a wide number of features obtained from the MER signal and compares six different classification algorithms trained using supervised learning. The used dataset was obtained from real surgery operations, comprises data from 14 PD patients who underwent DBS implantation, and is publicly available in ZENODO [21].

Appendix A. Spike-Dependent Features

Appendix A.1. Spike Firing Rate (SFR)

Defined in Equation (A1), where T is the time window (MER segment) and N_{sp} is the number of spike amplitudes during T.

$$SR = \frac{N_{sp}}{T} \tag{A1}$$

Appendix A.2. Inter-Spike Interval Sequences (ISI)

Defined by Equation (A2), where t_i Is the Occurrence Time of the *i*-th Spike in a Set of P Spikes.

$$ISI_i = t_{i+1} - t_i \quad i = 1, 2, \ldots, P - 1. \tag{A2}$$

Appendix A.3. Standard Deviation of ISI (SISI)

Defined by Equation (A3).

$$SISI = \sqrt{\frac{\sum_{i=1}^{N}\left(ISI_i - \overline{ISI}\right)^2}{n-1}} \tag{A3}$$

Appendix A.4. Pause Ratio (PR)

Defined by Equation (A4).

$$PR = \frac{\sum(ISI > 50\ ms)}{\sum(ISI < 50\ ms)} \tag{A4}$$

Appendix A.5. Pause Index (PI)

Defined by Equation (A5).

$$PI = \frac{\#(ISI > 50\ ms)}{\#(ISI < 50\ ms)} \tag{A5}$$

Appendix A.6. Bursting Rate (BR)

Defined by Equation (A6), where T is the time window (MER segment) and N_b is number of bursts during T.

$$BR = \frac{N_b}{T} \tag{A6}$$

Appendix A.7. Modified Burst Index (MBI)

Defined by Equation (A7),

$$MBI = \frac{\#(ISI < 10\ ms)}{\#(ISI > 10\ ms)} \tag{A7}$$

Appendix B. Spike-Independent Features

Let us consider that the MER segment samples are $s_i \in S, S = \{s_1, s_2, \ldots, s_N\}$, with N = 12,000 (1 s). The extracted features based on Local Field Potential are the following.

Appendix B.1. Bispectrum (Bs)

Bispectrum feature is derived from the degree of quadratic phase coupling between individual frequency components of the signal. First, the signal is divided into N samples; then, the Fourier transform on N samples is computed as the bispectrum component. Equation (A8) provides the details, where $B(f_1, f_2)$ is the bispectrum in the bifrequency (f_1, f_2), $S(f)$ is the discrete time Fourier transform of the given signal, $*$ denotes complex

conjugate, N is the sample per segment (in our study, $N = 8$), and (f_1 and f_2) values are defined from this interval range:

$$0 \leq f_2 \leq f_1 \leq f_s/2, f_1 + f_2 \leq f_s/2$$

where f_s is the sampling frequency.

$$Bs(f_1, f_2) = \sum_{i=1}^{N} S_j(f_1)S_j(f_2)S_j^*(f_1 + f_2) \tag{A8}$$

Appendix B.2. Zero Crossing (Zc)

Given in Equation (A9).

$$Zc = \sum_{i=1}^{N-1} |s_{i+1} - s_i| \tag{A9}$$

Appendix B.3. Curve Length (Cl)

Given in Equation (A10).

$$CL = \frac{3}{N-1} \sqrt{\sum_{i=1}^{N} (s_i - \bar{S})^2} \tag{A10}$$

Appendix B.4. Integrator (In)

Given in Equation (A11).

$$In = \frac{1}{2} \sum_{i=1}^{N-1} |\text{sign}(s_{i+1}) - \text{sign}(s_i)| \tag{A11}$$

Appendix B.5. Root Mean Square (RMS)

Given in Equation (A12).

$$RMS = \sqrt{\frac{1}{N} \sum_{i=1}^{N} s_i^2} \tag{A12}$$

Appendix B.6. Kurtosis (Ku)

Given in Equation (A13).

$$Ku = \frac{\frac{1}{N} \sum_{i=1}^{N} (s_i - \bar{S})^4}{\left(\frac{1}{N} \sum_{i=1}^{N} (s_i - \bar{S})^2 \right)^2} \tag{A13}$$

Appendix B.7. Cumulative Bispectrum (Cb)

Cumulative bispectrum is one of the robust methods applied for the non-stationary signals. By using the statistic moments: Equations (A14)–(A16), the higher-component statistics are computed as defined in Equations (A17)–(A19). In this work, only the third-order cumulants were considered.

$$m_1^s = E[S(k)] \tag{A14}$$

$$m_2^s = E[S(k)S(k+T)] \tag{A15}$$

$$m_3^s = E[S(k)S(k+T_1)S(k+T_2)] \tag{A16}$$

where T, T_1, and T_2 are the leg.

$$C_1^s = m_1^s \tag{A17}$$

$$C_2^s(T_1) = m_2^s(T_1) - (m_1^s)^2 \tag{A18}$$

$$Cb = C_3^s(T_1, T_2) = m_3^s(T_1, T_2) - m_1^s[m_2^s(T_1) + m_2^s(T_2) + m_2^s(T_2 - T_1)] + 2(m_1^s)^3 \tag{A19}$$

Appendix B.8. Average Amplitude Change (AAc)

Given in Equation (A20).

$$AAc = \frac{1}{N} \sum_{i=1}^{N-1} |s_{i+1} - s_i| \tag{A20}$$

Appendix B.9. Short-Term Fourier Transform (STFT)

Given in Equation (A21), with a windowing function $g(r)$.

$$STFT(f,k) = \sum_{r=1}^{N-1} s(t)g(t-k)\epsilon^{-j2\pi ft/N} \tag{A21}$$

where $STFT(f,k)$ is a complex-valued Fourier coefficient K is the window index. The frequency f, time t, and shift k are discrete.

Appendix B.10. Teager Energy (Te)

Given in Equation (A22).

$$Te = s^2[i] - s[i-1]s[i+1] \tag{A22}$$

Appendix B.11. Average First Amplitude Difference (AFa)

Given in Equation (A23).

$$AFa = \frac{1}{N} \sum_{k=1}^{N-1} |s_{k+1} - s_k| \tag{A23}$$

Appendix B.12. Second Amplitude Difference (SAd)

Given in Equation (A24).

$$SAd = \frac{1}{N} \sum_{k=1}^{N-1} |FA_{k+1} - FA_k| \tag{A24}$$

where FA is the difference between two successive samples (s_{n+1}, s_n). Then, $FA_i \in FA$, $FA = \{FA_1, FA_2, \ldots, FA_N\}$.

Appendix B.13. Standard Deviation (SD)

Given in Equation (A25).

$$STD = \sqrt{\frac{1}{N} \sum_{k=1}^{N} (s_k - \bar{s})^2} \tag{A25}$$

Appendix B.14. Skewness (Sk)

Given in Equation (A26).

$$Sk = \frac{\frac{1}{n} \sum_{i=1}^{N} (s_i - \bar{S})^3}{\left(\sqrt{\frac{1}{n} \sum_{i=1}^{N} (s_i - \bar{S})^2} \right)^3} \tag{A26}$$

Appendix B.15. Slope Sign Change (Sc)

Given in Equation (A27).

$$Sc = \sum_{i=1}^{N} f_{Sc}(s_i) \tag{A27}$$

where:

$$f_{Sc}(s_i) = \begin{cases} 1 & \text{if } s_i < s_{i+1} \text{ and } s_i < s_{i-1}, \text{ or } s_i < s_{i+1} \text{ and } s_i > s_{i-1} \\ 0 & \text{otherwise} \end{cases}$$

Appendix B.16. Variance (Va)

Given in Equation (A28).

$$\sigma = \frac{1}{N} \sum_{k=1}^{N} (s_k - \bar{S})^2 \tag{A28}$$
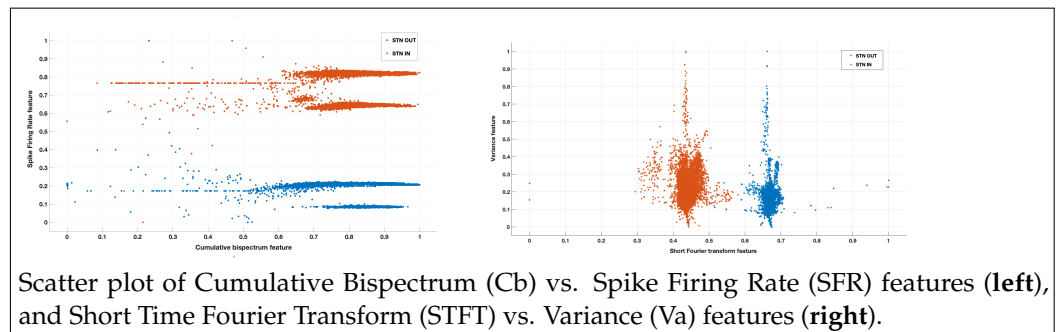
Appendix B.17. 1D-Local Binary Pattern (LBP1)

It brings the concepts used in 2D images into 1D signals. It compares the center values with its adjacent values as to produce a set of binary patterns according to a threshold. Thus, it is used to construct the final pattern as binary values converted to decimal values. The fundamental expression of *LBP*1 is given by Equation (A29), where
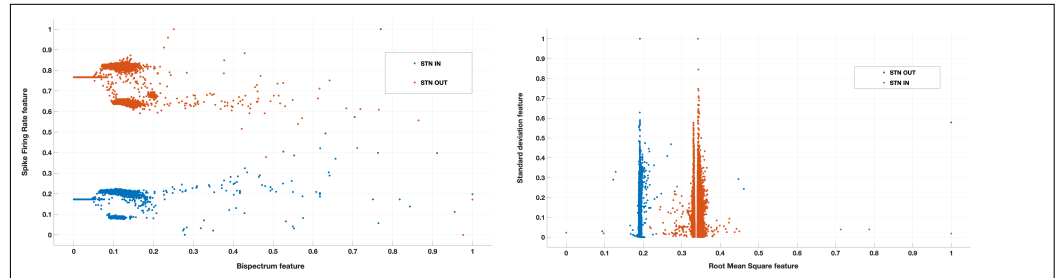
$$\text{sign}(s_i) = \begin{cases} 1 & \text{if } s_i \geq 0 \\ 0 & \text{otherwise} \end{cases}$$

and M_i and M_c represent the neighboring specific segment ($M_i = 9$) and center values ($M_c = 5$), respectively.

$$LBP1 = \sum_{i=0}^{N-1} \text{sign}(M_i - M_c) \cdot 2^i \tag{A29}$$

Appendix C. Scatter Plots for the Most Discriminant Features Used in the STN Area Detection
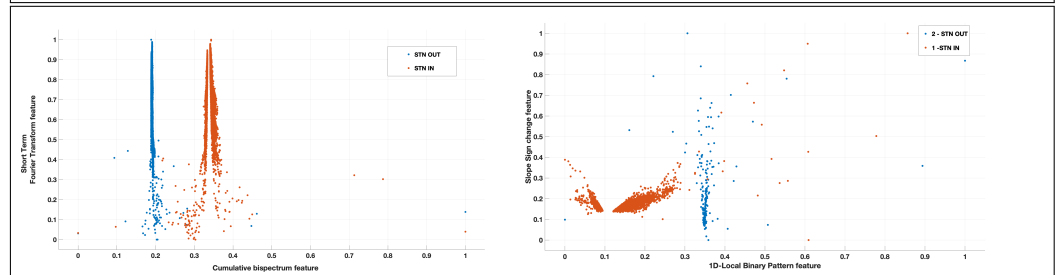

Scatter plot of Cumulative Bispectrum (Cb) vs. Spike Firing Rate (SFR) features (**left**), and Short Time Fourier Transform (STFT) vs. Variance (Va) features (**right**).

Scatter plot of Bispectrum (Bs) vs. Spike Firing Rate (SFR) features (**left**), and Root Mean Square (RMS) vs. Standard Deviation (SD) features (**right**).
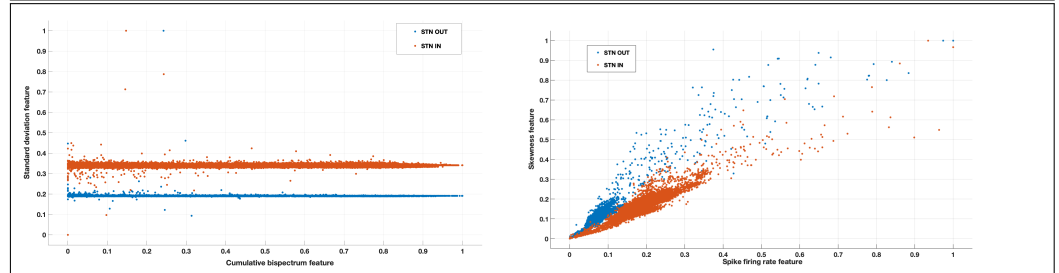

Scatter plot of Cumulative Bispectrum (Cb) vs. Standard Deviation (SD) features (**left**), and Spike Firing Rate (SFR) vs. Skewness (Sk) features (**right**).


Scatter plot of Cumulative Bispectrum (Cb) vs. Short Time Fourier Transform (STFT) features (**left**), and 1D_local binary Pattern (LBP1) vs. Slope Sign Change (SSc) features (**right**).
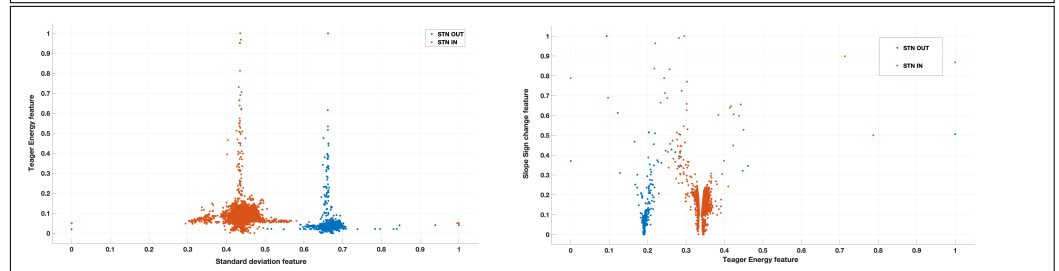
Scatter plot of Standard Deviation (SD) vs. Teager Energy (Te) features (**left**), and Teager Energy (Te) vs. Slope Sign Change (SSc) features (**right**).
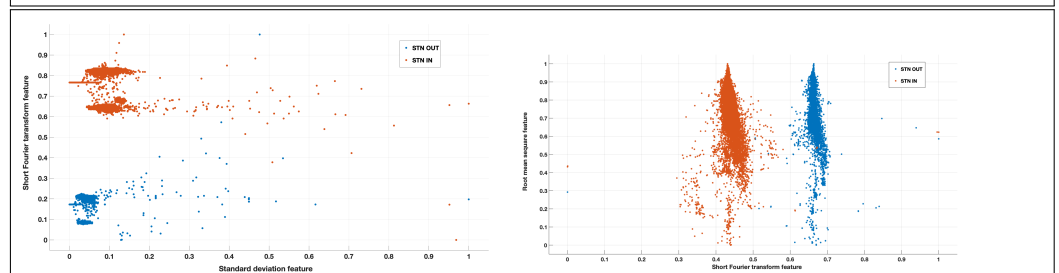
Scatter plot of Standard Deviation (SD) vs. Short Time Fourier Transform (STFT) features (**left**), and Short Time Fourier Transform (STFT) vs. Root Mean Square (RMS) features (**right**).

Scatter plot of vs. 1D_local binary Pattern (LBP1) features (**left**), and 1D_local binary Pattern (LBP1) vs. Variance (Va) features (**right**).

Scatter plot of Spike Firing Rate (SFR) vs. Variance (Va) features (**left**), and Standard Deviation (SD) vs. 1D_local binary Pattern (LBP1) features (**right**).
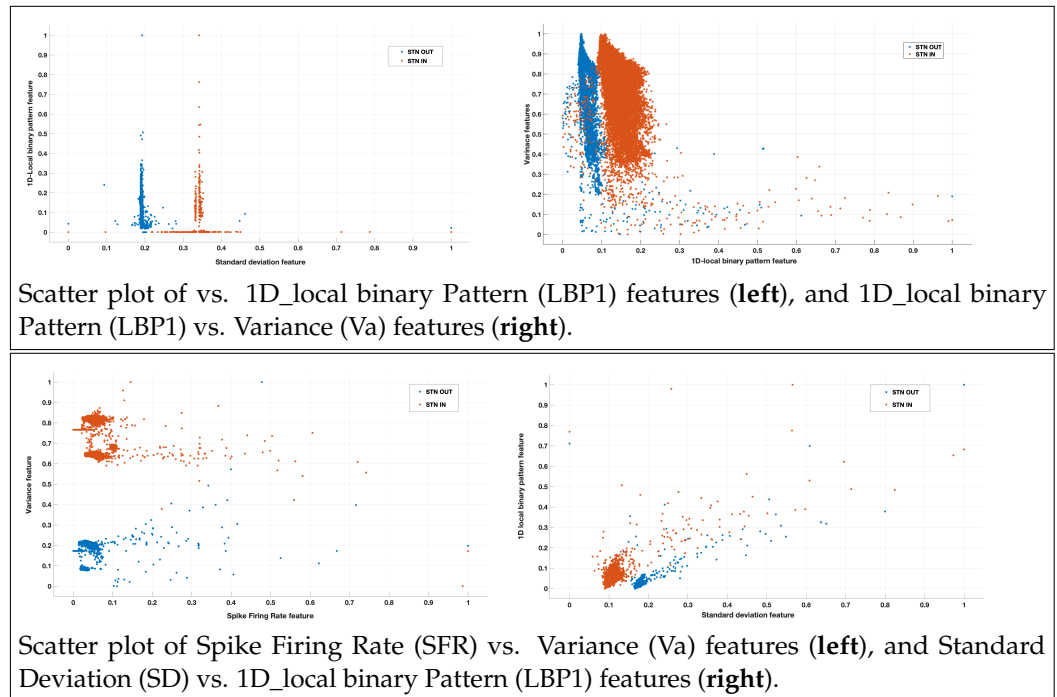
References

1. DeMaagd, G.; Philip, A. Parkinson's disease and its management: Part 1: Disease entity, risk factors, pathophysiology, clinical presentation, and diagnosis. *Pharm. Ther.* **2015**, *40*, 504.
2. Delamarre, A.; Meissner, W.G. Epidemiology, environmental risk factors and genetics of Parkinson's disease. *La Presse Médicale* **2017**, *46*, 175–181. [CrossRef] [PubMed]
3. Dorsey, E.R.; Elbaz, A.; Nichols, E.; Abbasi, N.; Abd-Allah, F.; Abdelalim, A.; Adsuar, J.C.; Ansha, M.G.; Brayne, C.; Choi, J.Y.J.; et al. Global, regional, and national burden of Parkinson's disease, 1990–2016: A systematic analysis for the Global Burden of Disease Study 2016. *Lancet Neurol.* **2018**, *17*, 939–953. [CrossRef] [PubMed]
4. Groiss, S.; Wojtecki, L.; Südmeyer, M.; Schnitzler, A. Deep brain stimulation in Parkinson's disease. *Ther. Adv. Neurol. Disord.* **2009**, *2*, 379–391. [CrossRef] [PubMed]
5. Martinez-Martin, P.; Skorvanek, M.; Henriksen, T.; Lindvall, S.; Domingos, J.; Alobaidi, A.; Kandukuri, P.L.; Chaudhari, V.S.; Patel, A.B.; Parra, J.C.; et al. Impact of advanced Parkinson's disease on caregivers: An international real-world study. *J. Neurol.* **2023**, *270*, 2162–2173. [CrossRef] [PubMed]
6. Lozano, C.S.; Tam, J.; Lozano, A.M. The changing landscape of surgery for Parkinson's Disease. *Mov. Disord.* **2018**, *33*, 36–47. [CrossRef] [PubMed]
7. Chen, Y.; Zhu, G.; Liu, Y.; Liu, D.; Yuan, T.; Zhang, X.; Jiang, Y.; Du, T.; Zhang, J. Predict initial subthalamic nucleus stimulation outcome in Parkinson's disease with brain morphology. *CNS Neurosci. Ther.* **2022**, *28*, 667–676. [CrossRef] [PubMed]
8. Chen, S.Y.; Tsai, S.T.; Hung, H.Y.; Lin, S.H.; Pan, Y.H.; Lin, S.Z. Targeting the Subthalamic Nucleus for Deep Brain Stimulation—A Comparative Study Between Magnetic Resonance Images Alone and Fusion with Computed Tomographic Images. *World Neurosurg.* **2011**, *75*, 132–137. [CrossRef]
9. Umemura, A.; Oka, Y.; Yamada, K.; Oyama, G.; Shimo, Y.; Hattori, N. Validity of Single Tract Microelectrode Recording in Subthalamic Nucleus Stimulation. *Neurol. Med.-Chir.* **2013**, *53*, 821–827. [CrossRef]
10. Wu, B.; Xu, J.; Zhang, C.; Ling, Y.; Yang, C.; Xuan, R.; Wang, S.; Guo, Q.; Zeng, Z.; Jiang, N.; et al. The Effect of Surgical Positioning on Pneumocephalus in Subthalamic Nucleus Deep Brain Stimulation Surgery for Parkinson Disease. *Neuromodul. Technol. Neural Interface* **2022**, *26*, 1714–1723. [CrossRef]
11. Vinke, R.S.; Geerlings, M.; Selvaraj, A.K.; Georgiev, D.; Bloem, B.R.; Esselink, R.A.; Bartels, R.H. The Role of Microelectrode Recording in Deep Brain Stimulation Surgery for Parkinson's Disease: A Systematic Review and Meta-Analysis. *J. Park. Dis.* **2022**, *12*, 2059–2069. [CrossRef] [PubMed]
12. Wan, K.R.; Maszczyk, T.; See, A.A.Q.; Dauwels, J.; King, N.K.K. A review on microelectrode recording selection of features for machine learning in deep brain stimulation surgery for Parkinson's disease. *Clin. Neurophysiol.* **2019**, *130*, 145–154. [CrossRef] [PubMed]
13. Tepper, Á.; Henrich, M.C.; Schiaffino, L.; Rosado Munoz, A.; Gutiérrez, A.; Guerrero Martinez, J. Selection of the optimal algorithm for real-time estimation of beta band power during DBS surgeries in patients with Parkinson's disease. *Comput. Intell. Neurosci.* **2017**, *2017*, 1512504. [CrossRef] [PubMed]

14. Karthick, P.; Wan, K.R.; Yuvaraj, R.; See, A.A.; King, N.K.K.; Dauwels, J. Detection of subthalamic nucleus using time-frequency features of microelectrode recordings and random forest classifier. In Proceedings of the 2019 41st Annual International Conference of the IEEE Engineering in Medicine and Biology Society (EMBC), Berlin, Germany, 23–27 July 2019; pp. 4164–4167.

15. Lourens, M.; Meijer, H.; Contarino, M.; Van den Munckhof, P.; Schuurman, P.; Van Gils, S.; Bour, L. Functional neuronal activity and connectivity within the subthalamic nucleus in Parkinson's disease. *Clin. Neurophysiol.* **2013**, *124*, 967–981. [CrossRef] [PubMed]

16. Novak, P.; Przybyszewski, A.W.; Barborica, A.; Ravin, P.; Margolin, L.; Pilitsis, J.G. Localization of the subthalamic nucleus in Parkinson disease using multiunit activity. *J. Neurol. Sci.* **2011**, *310*, 44–49. [CrossRef]

17. Hosny, M.; Zhu, M.; Su, Y.; Gao, W.; Fu, Y. A novel deep recurrent convolutional neural network for subthalamic nucleus localization using local field potential signals. *Biocybern. Biomed. Eng.* **2021**, *41*, 1561–1574. [CrossRef]

18. Rajpurohit, V.; Danish, S.F.; Hargreaves, E.L.; Wong, S. Optimizing computational feature sets for subthalamic nucleus localization in DBS surgery with feature selection. *Clin. Neurophysiol.* **2015**, *126*, 975–982. [CrossRef] [PubMed]

19. Hosny, M.; Zhu, M.; Gao, W.; Fu, Y. Detection of subthalamic nucleus using novel higher-order spectra features in microelectrode recordings signals. *Biocybern. Biomed. Eng.* **2021**, *41*, 704–716. [CrossRef]

20. Hosny, M.; Zhu, M.; Gao, W.; Fu, Y. Deep convolutional neural network for the automated detection of Subthalamic nucleus using MER signals. *J. Neurosci. Methods* **2021**, *356*, 109145. [CrossRef]

21. Rosado-Muñoz, A.; Guerrero-Martínez, J.F.; Gutierrez Martín, A. Microelectrode register (MER) data from Deep Brain Stimulation (DBS) surgery in Parkinson's disease patients. DATASET. *Zenodo* **2022**. [CrossRef]

22. Toosi, R.; Akhaee, M.A.; Dehaqani, M.R.A. An automatic spike sorting algorithm based on adaptive spike detection and a mixture of skew-t distributions. *Sci. Rep.* **2021**, *11*, 13925. [CrossRef] [PubMed]

23. Schwalger, T. The Interspike-Interval Statistics of Non-Renewal Neuron Models. Ph.D. Thesis, Humboldt-Universität zu Berlin, Berlin, Germany, 2013. [CrossRef]

24. Toledo-Pérez, D.C.; Rodríguez-Reséndiz, J.; Gómez-Loenzo, R.A.; Jauregui-Correa, J. Support vector machine-based EMG signal classification techniques: A review. *Appl. Sci.* **2019**, *9*, 4402. [CrossRef]

25. Yuvaraj, R.; Rajendra Acharya, U.; Hagiwara, Y. A novel Parkinson's Disease Diagnosis Index using higher-order spectra features in EEG signals. *Neural Comput. Appl.* **2018**, *30*, 1225–1235. [CrossRef]

26. Caesarendra, W.; Tjahjowidodo, T. A Review of Feature Extraction Methods in Vibration-Based Condition Monitoring and Its Application for Degradation Trend Estimation of Low-Speed Slew Bearing. *Machines* **2017**, *5*, 21. [CrossRef]

27. Yahyaei, R.; Özkurt, T.E. Mean curve length: An efficient feature for brainwave biometrics. *Biomed. Signal Process. Control* **2022**, *76*, 103664. [CrossRef]

28. Sharma, L.; Dandapat, S.; Mahanta, A. Kurtosis-based noise estimation and multiscale energy to denoise ECG signal. *Signal, Image Video Process.* **2013**, *7*, 235–245. [CrossRef]

29. Yuegang, W.; Shao, J.; Hongtao, X. Non-stationary Signals Processing Based on STFT. In Proceedings of the 2007 8th International Conference on Electronic Measurement and Instruments, Xi'an, China, 16–18 August 2007; pp. 3-301–3-304. [CrossRef]

30. Choi, J.H.; Jung, H.K.; Kim, T. A new action potential detector using the MTEO and its effects on spike sorting systems at low signal-to-noise ratios. *IEEE Trans. Biomed. Eng.* **2006**, *53*, 738–746. [CrossRef] [PubMed]

31. Attallah, B.; Serir, A.; Chahir, Y. Feature extraction in palmprint recognition using spiral of moment skewness and kurtosis algorithm. *Pattern Anal. Appl.* **2019**, *22*, 1197–1205. [CrossRef]

32. Benouis, M.; Mostefai, L.; Costen, N.; Regouid, M. ECG based biometric identification using one-dimensional local difference pattern. *Biomed. Signal Process. Control* **2021**, *64*, 102226. [CrossRef]

33. Houam, L.; Hafiane, A.; Boukrouche, A.; Lespessailles, E.; Jennane, R. One dimensional local binary pattern for bone texture characterization. *Pattern Anal. Appl.* **2014**, *17*, 179–193. [CrossRef]

34. Yang, W.; Wang, K.; Zuo, W. Neighborhood component feature selection for high-dimensional data. *J. Comput.* **2012**, *7*, 161–168. [CrossRef]

35. Paluszek, M.; Thomas, S.; Paluszek, M.; Thomas, S. MATLAB machine learning toolboxes. In *Practical MATLAB Deep Learning: A Project-Based Approach*; Apress: Berkeley, CA, USA, 2020; pp. 25–41.

36. Chaovalitwongse, W.A.; Jeong, Y.S.; Jeong, M.K.; Danish, S.F.; Wong, S. Pattern recognition approaches for identifying subcortical targets during deep brain stimulation surgery. *IEEE Intell. Syst.* **2011**, *26*, 54–63. [CrossRef]

37. Wong, S.; Baltuch, G.; Jaggi, J.; Danish, S. Functional localization and visualization of the subthalamic nucleus from microelectrode recordings acquired during DBS surgery with unsupervised machine learning. *J. Neural Eng.* **2009**, *6*, 026006. [CrossRef]

38. Cagnan, H.; Dolan, K.; He, X.; Contarino, M.F.; Schuurman, R.; Van Den Munckhof, P.; Wadman, W.J.; Bour, L.; Martens, H.C. Automatic subthalamic nucleus detection from microelectrode recordings based on noise level and neuronal activity. *J. Neural Eng.* **2011**, *8*, 046006. [CrossRef] [PubMed]

39. Guillén, P.; Martinez-de Pison, F.; Sanchez, R.; Argáez, M.; Velázquez, L. Characterization of subcortical structures during deep brain stimulation utilizing support vector machines. In Proceedings of the 2011 Annual International Conference of the IEEE Engineering in Medicine and Biology Society, Boston, MA, USA, 30 August–3 September 2011; pp. 7949–7952.

40. Padilla, J.; Vargas Cardona, H.; Arango, A.; Carmona, H.; Álvarez, M.; Guijarro, E.; Orozco, A. NEUROZONE: On-line recognition of brain structures in stereotactic surgery–Application to Parkinson's disease surgery. In Proceedings of the 2012 Annual International Conference of the IEEE Engineering in Medicine and Biology Society, San Diego, CA, USA, 28 August–1 September 2012.

41. Schiaffino, L.; Muñoz, A.R.; Martínez, J.G.; Villora, J.F.; Gutiérrez, A.; Torres, I.M. STN area detection using K-NN classifiers for MER recordings in Parkinson patients during neurostimulator implant surgery. In *Proceedings of the Journal of Physics: Conference Series*; IOP Publishing: Bristol, UK, 2016; Volume 705, p. 012050.

42. Schiaffino, L.; Rosado Muñoz, A.; Francés Villora, J.; Bataller, M.; Gutiérrez, A.; Martínez Torres, I.; Teruel-Martí, V.; Guerrero Martínez, J. Feature selection for KNN classifier to improve accurate detection of subthalamic nucleus during deep brain stimulation surgery in Parkinson's patients. In *VII Latin American Congress on Biomedical Engineering CLAIB 2016, Bucaramanga, Santander, Colombia, 26–28 October 2016*; Torres, I., Bustamante, J., Sierra, D.A., Eds.; Springer: Singapore, 2017; pp. 441–444. [CrossRef]

43. Valsky, D.; Marmor-Levin, O.; Deffains, M.; Eitan, R.; Blackwell, K.T.; Bergman, H.; Israel, Z. Stop! border ahead: A utomatic detection of subthalamic exit during deep brain stimulation surgery. *Mov. Disord.* **2017**, *32*, 70–79. [CrossRef] [PubMed]

44. Bellino, G.M.; Schiaffino, L.; Battisti, M.; Guerrero, J.; Rosado-Muñoz, A. Optimization of the KNN supervised classification algorithm as a support tool for the implantation of deep brain stimulators in patients with Parkinson's disease. *Entropy* **2019**, *21*, 346. [CrossRef]

45. Khosravi, M.; Atashzar, S.F.; Gilmore, G.; Jog, M.S.; Patel, R.V. Unsupervised clustering of micro-electrophysiological signals for localization of subthalamic nucleus during DBS surgery. In Proceedings of the 2019 9th International IEEE/EMBS Conference on Neural Engineering (NER), San Francisco, CA, USA, 20–23 March 2019; pp. 17–20.

46. Khosravi, M.; Atashzar, S.F.; Gilmore, G.; Jog, M.S.; Patel, R.V. Intraoperative localization of STN during DBS surgery using a data-driven model. *IEEE J. Transl. Eng. Health Med.* **2020**, *8*, 1–9. [CrossRef] [PubMed]

47. Karthick, P.; Wan, K.R.; Qi, A.S.A.; Dauwels, J.; King, N.K.K. Automated detection of subthalamic nucleus in deep brain stimulation surgery for Parkinson's disease using microelectrode recordings and wavelet packet features. *J. Neurosci. Methods* **2020**, *343*, 108826. [CrossRef]

48. Coelli, S.; Levi, V.; Del Vecchio, J.D.V.; Mailland, E.; Rinaldo, S.; Eleopra, R.; Bianchi, A.M. An intra-operative feature-based classification of microelectrode recordings to support the subthalamic nucleus functional identification during deep brain stimulation surgery. *J. Neural Eng.* **2021**, *18*, 016003. [CrossRef]

49. Vinke, R.S.; Selvaraj, A.K.; Geerlings, M.; Georgiev, D.; Sadikov, A.; Kubben, P.L.; Doorduin, J.; Praamstra, P.; Bloem, B.R.; Bartels, R.H.; et al. The Role of Microelectrode Recording and Stereotactic Computed Tomography in Verifying Lead Placement during Awake MRI-Guided Subthalamic Nucleus Deep Brain Stimulation for Parkinson's Disease. *J. Park. Dis.* **2022**, *12*, 1269–1278. [CrossRef]

50. Watts, J.; Khojandi, A.; Shylo, O.; Ramdhani, R.A. Machine learning's application in deep brain stimulation for Parkinson's disease: A review. *Brain Sci.* **2020**, *10*, 809. [CrossRef] [PubMed]

51. Koirala, N.; Serrano, L.; Paschen, S.; Falk, D.; Anwar, A.R.; Kuravi, P.; Deuschl, G.; Groppa, S.; Muthuraman, M. Mapping of subthalamic nucleus using microelectrode recordings during deep brain stimulation. *Sci. Rep.* **2020**, *10*, 19241. [CrossRef] [PubMed]

52. Martin, T.; Peralta, M.; Gilmore, G.; Sauleau, P.; Haegelen, C.; Jannin, P.; Baxter, J.S. Extending convolutional neural networks for localizing the subthalamic nucleus from micro-electrode recordings in Parkinson's disease. *Biomed. Signal Process. Control* **2021**, *67*, 102529. [CrossRef]